Autocorrelation of the ground vibrations recorded by the SEIS-InSight seismometer on Mars.

N. Compaire[1], L. Margerin[2], R.F. Garcia[1,2], B. Pinot[1], M. Calvet[2], G. Orhand-Mainsant[1], D. Kim[9], V. Lekic[9], B. Tauzin[11,12], M. Schimmel[10], E. Stutzmann[4], B. Knapmeyer-Endrun[5], P. Lognonné[4], W. T. Pike [6], N. Schmerr[9], L. Gizon [8], W. B. Banerdt[7]

[1]Institut Supérieur de l'Aéronautique et de l'Espace SUPAERO, 10 Avenue Edouard Belin, 31400 Toulouse, France
[2]Institut de Recherche en Astrophysique et Planétologie, Université Toulouse III Paul Sabatier, CNRS, CNES, 14 Av. E. Belin, 31400, Toulouse, France
[4]Université de Paris, Institut de physique du globe de Paris, CNRS, F-75005 Paris, France
[5]Bensberg Observatory, University of Cologne, Vinzenz-Pallotti-Str. 26, 51429 Bergisch Gladbach, Germany
[6]Department of Electrical and Electronic Engineering, Imperial College London, South Kensington Campus, London, SW7 2AZ, United Kingdom
[7]Jet Propulsion Laboratory, California Institute of Technology, Pasadena, CA 91109, USA
[8]Max Planck Institute for Solar System Research, Justus-von-Liebig-Weg 3, 37077 Göttingen, Germany
[9]University of Maryland, College Park, Department of Geology, 8000 Regents Dr., College Park, MD, 20742, USA
[10]Institute of Earth Sciences Jaume Almera – CSIC, Barcelona, Spain
[11]Université de Lyon, Université Claude Bernard Lyon 1, ENS, CNRS, Laboratoire de Géologie de Lyon : Terre, Planètes, Environnement, 69622 Villeurbanne, France
[12]Research School of Earth Sciences, The Australian National University, Canberra, Australian Capital Territory 0200, Australia

Key Points:

- Autocorrelation functions of SEIS background noise and seismic events are computed and validated by inter-comparison
- Stable background seismic noise autocorrelation is observed only at 2.4 Hz resonance peak
- Various arrivals are observed in autocorrelation functions and interpreted as seismic reflections

Corresponding author: Nicolas Compaire, nicolas.compaire@isae-supaero.fr

Abstract

The SEIS seismometer of the InSight mission was deployed on the ground of Elysium Planitia, on 19 December 2018. Interferometry techniques can be used to extract information on the internal structure from the autocorrelation of seismic ambient noise and coda of seismic events. In a single-station configuration, the zero-offset global reflection of the ground vertically below the seismometer can be approximated by the stacked ZZ autocorrelation function (ACF) for P-waves and the stacked EE and NN ACFs for S-waves, assuming a horizontally layered medium and homogeneously distributed and mutually uncorrelated noise sources. We analyze continuous records from the very broadband seismometer (SEIS-VBB), and correct for potential environmental disturbances through systematic preprocessing. For each Sol (martian day), we computed the correlations functions in 24 windows of one martian hour in order to obtain a total correlation tensor for various Mars local times. In addition, a similar algorithm is applied to the Marsquake waveforms in different frequency bands. Both stability analysis and inter-comparison between background noise and seismic event results suggest that the background seismic noise at the landing site is reliably observed only around 2.4 Hz, where an unknown mechanism is amplifying the ground shaking, and only during early night hours, when the noise induced by atmospheric disturbances is minimum. Seismic energy arrivals are consistently observed across the various data-sets. Some of these arrivals present multiples. These observations are discussed in terms of Mars' crustal structure.

Plain Language Summary

The correlation of seismic records is the basis of seismic interferometry methods. These methods use the seismic waves, either from background vibrations of the planet or from quakes, that are scattered in the medium in order to recover information about structure between two seismic sensors. SEIS seismometer on board InSight NASA Discovery Mars mission being a single instrument, the recordings of ground velocity in the 3 space directions can only be correlated with themselves. A method is implemented to compute reliably these correlations using SEIS records. The comparison of the results obtained for seismic shaking to the ones obtained for background vibrations demonstrates that the background seismic noise is above the self-noise of SEIS only during early night hours, and only around a specific frequency (2.4 Hz). The seismic vibrations appears to be amplified at this frequency by an unknown mechanism. Some seismic energy arrivals appears consistently, at specific propagation times, between the various data sets and processing parameters tested. These arrivals are interpreted as vertically propagating seismic waves which are reflected on top of crustal layers. Their propagation times can be used to constrain a model of Mars' crustal structure.

1 INTRODUCTION

NASA's InSight (Interior Exploration using Seismic Investigations, Geodesy and Heat Transport) mission landed on November, 26th 2018 near the martian equator in Elysium Planitia (Banerdt et al., 2020). The seismological records of its main instrument SEIS (Seismic Experiment for Interior Structure) present a dataset of unprecedented quality for planetary seismology. The instrument's capabilities and the extremely low amplitude of the ambient ground vibrations on Mars make the recorded signal very different compared to Earth's seismic data (Lognonné et al., 2019). Not all the features of the ground velocity records can be interpreted as seismic signals, and all the details of the InSight mission system have to be taken into account to correctly interpret the data. Among these, we can mention the lander-related noise, the electrical noise, the atmospheric noise and all the mechanical resonances that are temperature dependent (Murdoch, Mimoun, et al., 2017; Murdoch, Kenda, et al., 2017; Lognonné et al., 2020). Henceforth, we refer to these as "environmental noise".

One powerful tool for planetary seismology is the analysis of passively-observed signals created by natural processes such as wind, earthquakes, etc. Planetary bodies like the Moon or Mars have a much lower seismicity rate compared to Earth due to the absence of plate tectonic. As a consequence, the scarcity and low amplitude of seismic sources can be an issue for seismological applications. The capability of passive seismic interferometry methods to extract information from seismic ambient noise and diffuse wavefields is thus of great interest.

Seismic interferometry has been applied with success on the Moon by Larose (2005). They performed subsurface tomography with shear waves extracted between stations of the Apollo array from Lunar ambient noise. This approach allowed them to glean new insights from an already prolific dataset. More recently Nishitsuji et al. (2016) performed single-station autocorrelations on Apollo's records to retrieve body-waves reflected in the Lunar crust. Since the work by Claerbout (1968), we know that correlating a single-station records with themselves allows us to estimate the reflection response of the ground vertically beneath the seismometer. This theoretical result obtained for 1D-horizontally layered mediums has been extended for 3D-inhomogeneous medium by Wapenaar (2003). Thereafter many studies applied this principle on real data to investigate the Earth's crust (Tibuleac & von Seggern, 2012; Ito & Shiomi, 2012; Gorbatov et al., 2013; Kennett et al., 2015; Saygin et al., 2017; Phạm & Tkalčić, 2017; Oren & Nowack, 2017; Romero & Schimmel, 2018). Single station autocorrelations have also been used extensively for monitoring, in a variety of settings, for velocity changes due to precipitation, groundwater or thermal forcing in Wegler and Sens-Schönfelder (2007); Kim and Lekic (2019).

In this study, we apply the same imaging approach to data from the InSight very broadband seismometer SEIS-VBB to investigate the structure of the martian crust beneath InSight's landing site. The reconstructed reflection response from single-station seismic interferometry brings some information which, combined with other methods such as receiver functions and seismic waveform analysis, can constrain very precisely the depth of the crust-mantle boundary of Mars. The determination of this depth is one of the main goals of the InSight mission.

The study of the seismic background recorded by SEIS can also bring useful information to the other goals of SEIS. Indeed, in the context of the InSight mission the identification of the sources of signals recorded by SEIS is critical for the study of the seismicity. A relatively small number of the events detected by SEIS can be clearly identified as Marsquakes because they present clear phases arrivals, but for the majority of transient signals in the dataset the interpretation is much more complicated. A large number of these transients seems to be related to a mysterious continuous resonance around 2.4 Hz. The interpretation of these events as Marsquakes depends on the physical phenomenon that we consider responsible for this resonance. The study and the characterization of the ambient seismic noise recorded by SEIS is thus a critical point for all the seismological analyses underlying the mission requirements (Lognonné et al., 2019).

In section 2, we describe the particular features of the continuous records of SEIS-VBB and the various types of seismic events. We present the pre-processing used to deal with the environmental disturbances and the methodology applied to compute the autocorrelation functions and their signal-to-noise ratio. In section 3, we present and compare the results obtained on seismic ambient noise and seismic event waveforms. In section 4, we discuss the potential remaining contaminations and the interpretation of observed phase arrivals in terms of crustal structure.

2 DATA AND METHOD

2.1 Description of SEIS and data used

SEIS is one of the main instruments of the InSight mission (InSight Mars SEIS Data Service, 2019). It is a six axes seismometer composed of three Very Broad Band (VBB) seismometers and three Short Period (SP) seismometers. The three VBB axes provide two types of output : a velocity (VEL) output sensitive to frequencies between 0.01Hz and 20Hz and a position (POS) output sensitive to frequencies lower than 0.1Hz. The three SP axes are sensitive to frequencies between 0.01Hz and 50Hz (Lognonné et al., 2019).

SEIS was deployed on the martian surface with the robotic arm of InSight lander on 19 December 2018. It has been covered by its Wind and Thermal Shield (WTS) since 2 February 2019 (Lognonné et al., 2020). SEIS is continuously recording ground motion at the InSight's landing site. The data flow is composed of continuous data at low sampling rates and event data at high sampling rates. The sampling rate of continuous channels of SEIS has varied during the first year of operation. Between February 2019 and May 2019 the VBB continuous data flow for the high gain velocity output was at 2 samples-per-second (sps) and then at 10 sps. During the same time period, the SP continuous data flow for the high gain output was also at 2sps and 10sps. Since June, 2019 the continuous channels are available at 20sps for both the VBB and the SP, excluding the Mars conjunction period during which SEIS was turned off.

As will be described in the following section both the high ($>$ 10Hz) and low ($<$ 1Hz) frequency bands of these records are contaminated by transient signals that are able to clearly distort the results of passive seismic techniques. Nevertheless those on the low frequency band (called glitches) are less numerous and have been the subject of more works in order to remove them (Lognonné et al., 2020; Scholz et al., 2020). For these reasons we focused our analysis on the frequency band below 10Hz and chose to use VBB data at 10 and 20 sps, since it is less noisy than SP data in this frequency band.

2.2 Description of the continuous signal

The continuous records of SEIS present several features that have been described in Lognonné et al. (2020). We briefly summarize its mains characteristics here. We show in Figure 1.A a spectrogram of raw records of the VBB axes at 20 sps. The periods with the highest energy correspond to the sunlight periods of the various Sols. This day-night distinction in the noise level is controlled by atmospheric processes. As described by Lognonné et al. (2020) (Supplementary Discussion 1) this atmospheric noise comprises elastic ground deformations induced by pressure effects on the ground, tilt of the lander under wind and lander vibrations under wind. The changes in the speed and the turbulent flow of the wind are the main drivers of the SEIS background signal.

Next, we can notice that these high energetic bands varying with times. Some of them are framed in the red rectangle of the Figure 1.A. These bands correspond to the various modes of resonance of the InSight lander. Indeed, lander vibrations are continuously excited by the wind. Its various components resonate in different frequency bands that are determined by the physical properties of its mechanical parts (Murdoch, Mimoun, et al., 2017). As these physical properties are temperature-sensitive, we observe changes in the frequencies of these resonances that follow the temperature variations at the InSight landing site. These lander modes are distributed over the 1-50 Hz frequency band and some of them are strongly polarized either on the horizontal components or on the vertical component.

We can also observed on Figure 1.A (black rectangles) a constant excitation between 2Hz and 3Hz that do not vary with time. This feature is called the "2.4Hz resonance" and is interpreted by Giardini et al. (2020) as a local ground resonance. Nevertheless, many questions remain on its origin.

On the spectrogram of the Figure 1.A we also notice a horizontal line at exactly 1Hz. This feature is more clearly visible on the corresponding mean amplitude spectrum shown on Figure 1.B. We see the main peak at 1Hz and the various harmonics at 2Hz, 3Hz, etc. These harmonics are not all visible on the spectrogram due to a resolution issue on the image. This signal, called "tick-noise", is a periodic cross-talk induced by the acquisition of the temperature sensors at 1 sps. The temperature sensors and the seismometer axes being managed by the same clock, the cross-talk signal on SEIS records is thus perfectly synchronized with SEIS signals.

The two last features in the records of SEIS are presented on Figure 2. They are two types of transient disturbances. One of them dominates the low frequency band and is referred to as "glitch" (panels 2.A and 2.B)). The other dominates the high frequency band and is referred to as "donk" (panels 2.C and 2.D). The most likely origin of these transients is the occurrence of cracks in the various mechanical parts of the InSight station including the lander, the Sensor Assembly (SA) of SEIS and the tether between SEIS and the lander. Indeed, the temperature variation between day and night at the InSight landing site can reach 100K. All the mechanical parts are thus subject to high thermal stresses that can create such cracks.

All of these features can adversely affect the results of the seismic interferometry and are the subject of several data procedures described in part 2.4.

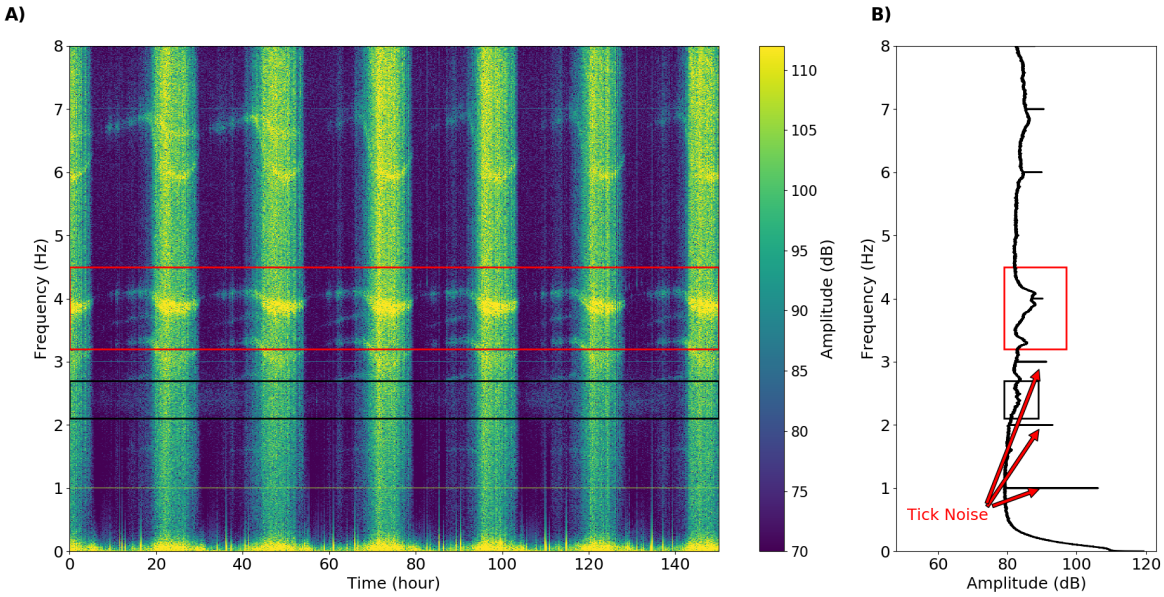

Figure 1. A) Spectrogram of a 6 Sols-long record of raw 20 sps VBB data (component V). The vertical bands of high amplitude correspond to daytime windows, i.e. between 3:00 and 16:00 LMST (Local Mean Solar Time). Due to image resolution issue, all the tick-noise harmonics are not visible on the spectrogram. B) Mean amplitude spectrum (dB) of the same data. The red rectangles on both A) and B) show several lander modes around 4Hz. The black rectangles show the location of the 2.4Hz resonance.

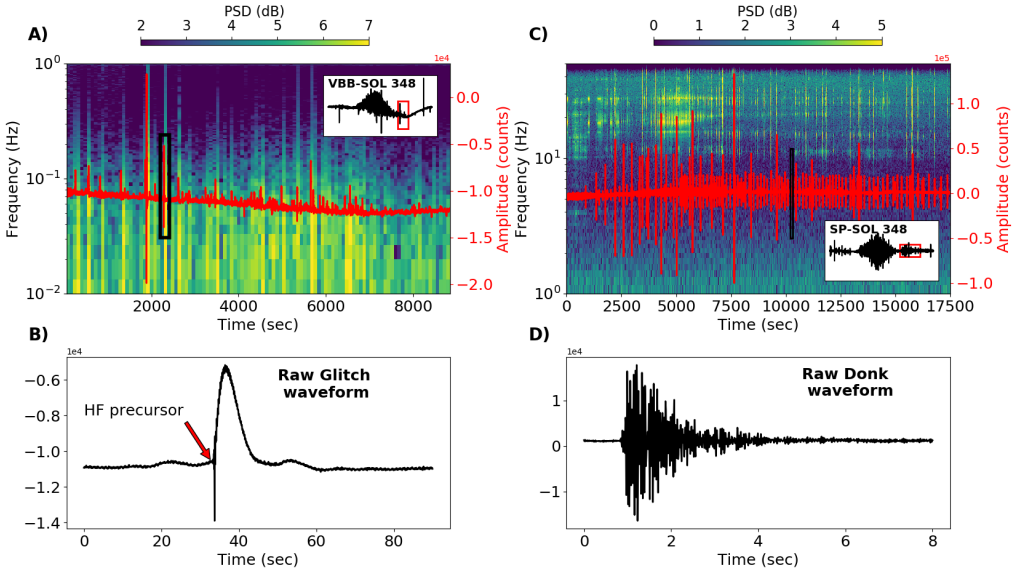

Figure 2. A) Spectrogram of raw VBB-V component at 20sps at the beginning of the evening of Sol 348. Each high energy peak in the low frequency band is the signature of a glitch. They are also clearly visible in the temporal domain (red line). The black rectangle correspond to the time window of the glitch presented in the subplot B). We show in the thumbnail the whole record of Sol 348 for VBB. The red rectangle correspond to the time window of the spectrogram. B) Typical raw glitch waveform. C) Spectrogram of raw SP2 (horizontal) component-100sps-SP data during the evening of Sol 348. Each high energy peak in the high frequency band is the signature of a donk. They are also clearly visible in the time domain (red line). The black rectangle correspond to the time window of the donk presented in the subplot D). We show in the thumbnail the whole record of Sol 348 for SP2. The red rectangle correspond to the time window of the spectrogram. D) Typical raw donk waveform.

2.3 Description of events characteristics

Since the beginning of the operation phase SEIS has recorded more than a hundred events (Giardini et al., 2020). The event nomenclature used in this study refers to the catalogue provided by the MarsQuake Service (MQS) (InSight Marsquake Service, 2020) described in Giardini et al. (2020). The events are classified into four types and have an assigned quality score from A (best) to D (worst). An example of spectral content for each type of event is presented in Figure 3. We note that the peak of the 2.4Hz resonance is present in all the noise windows used for comparison. The events that only excite the 2.4Hz resonance are called "2.4Hz events". The events that also have some energy at frequencies higher than around 2.4Hz are called "High Frequency events" (HF) or "Very High Frequency events" (VHF) when the partitioning of the energy between the horizontal and vertical components is well marked. The events that excite the 2.4Hz resonance, but with the major part of their energy at lower frequencies, are called "Broad-Band events" (BB). Finally, the events with energy exclusively below the 2.4Hz resonance are called "Low Frequency events" (LF).

In this study, we have performed autocorrelation of Marsquake waveforms in various frequency bands. In all, we have used seven LF, five BB, fifty-five HF-VHF and sixty-nine 2.4Hz events. We have only selected seismic events of quality A, B and C. As described by Giardini et al. (2020), the waveforms of the detected seismic events have a

diffusive character. In this study, we use the coda of seismic events starting after the S wave arrival. However, a clear identification of the P and S phases is only possible for the events with the highest quality (A or B). As a consequence, the time-window used for the computation of the autocorrelation function depends on the presence of a clear S-wave phase. We use for this purpose the phase picks provided by the MQS catalogue. By default the time-window is defined as the whole event's time-window defined in the catalogue. When an *S*-wave phase has been picked, we use this arrival time as the beginning of the time-window.

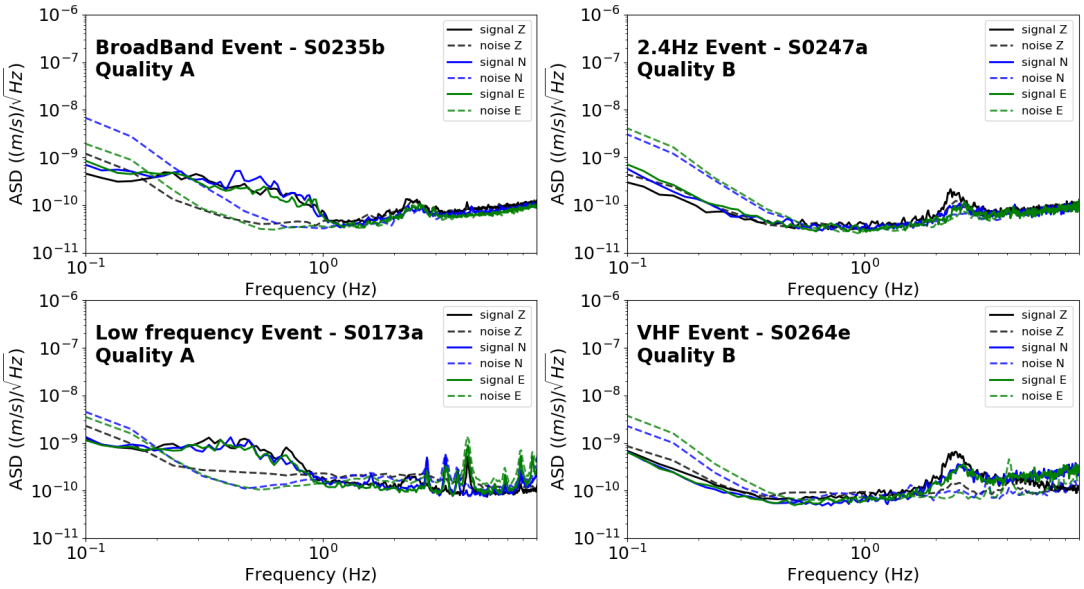

Figure 3. Amplitude Spectral Density (ASD) during the time window of the seismic event compared to the ASD of the noise for the three VBB components. The denomination of the events and their quality label follows the classification of the Marsquake Service (MQS). The various high-frequency peaks visible on the ASD of the LF event S0173a are due to lander modes. Depending on the local solar time at the InSight's landing site during the occurence of an event, the lander modes are more or less apparent on the spectra.

2.4 Processing

2.4.1 Pre-processing : Removing the tick-noise

The tick-noise is an electrical disturbance (cross-talk) coming from the acquisition of the temperature sensor inside the SEIS instrument so that the frequency of this signal depends on the sampling rate of the temperature sensor. This sampling rate has changed since the beginning of the operation phase from 0.1 sps to 1 sps, but for the most part of the period until the date of this study it was equal to 1 sps. The tick-noise is not a pulse. It has a waveform that is different for the three channels U, V and W of the VBB. As the acquisition of the temperature sensor is synchronized with the acquisition of the seismic channels, this waveform repeats periodically on the various seismic channels with a number of sample exactly equal to the sampling rate of the SEIS channel. This means that it is not sensitive to temporal drift. As observed in Figure 1, the tick-noise presents

a fundamental frequency at 1Hz but also a non-zero amplitude at each harmonic (2Hz, 3Hz, ...). In order to remove it from the raw data at 20sps, we stack non-overlapping contiguous 20-samples windows. Under the assumption that the background noise is random, the stack should converge towards a good estimate of the tick-noise waveform. To obtain the estimates presented in the Figure 4.A, we use two months of 20 sps VBB records during the early night. We use only evening data (between 18:00 and 22:00 LMST) because it is the least noisy period. To remove the estimated tick-noise from the time-series we correlate it with the tick-noise waveform. The location of the maximum informs us on the lag-time between the estimated waveform and the tick-noise for the given time-series. We can then correctly synchronise the estimated tick-noise waveform with the time-series and remove the former from the latter in contiguous windows of 20 samples by subtraction. Figure 4.B shows the spectrograms around the fundamental at 1Hz before and after the tick-noise removal for each component. Figure 4.C and 4.D show the time-series and the spectral contents of VBB-V for the evening part of Sol 183 before and after the tick-noise removal. We see that the tick-noise signature is removed and that the rest of the spectral content is preserved.

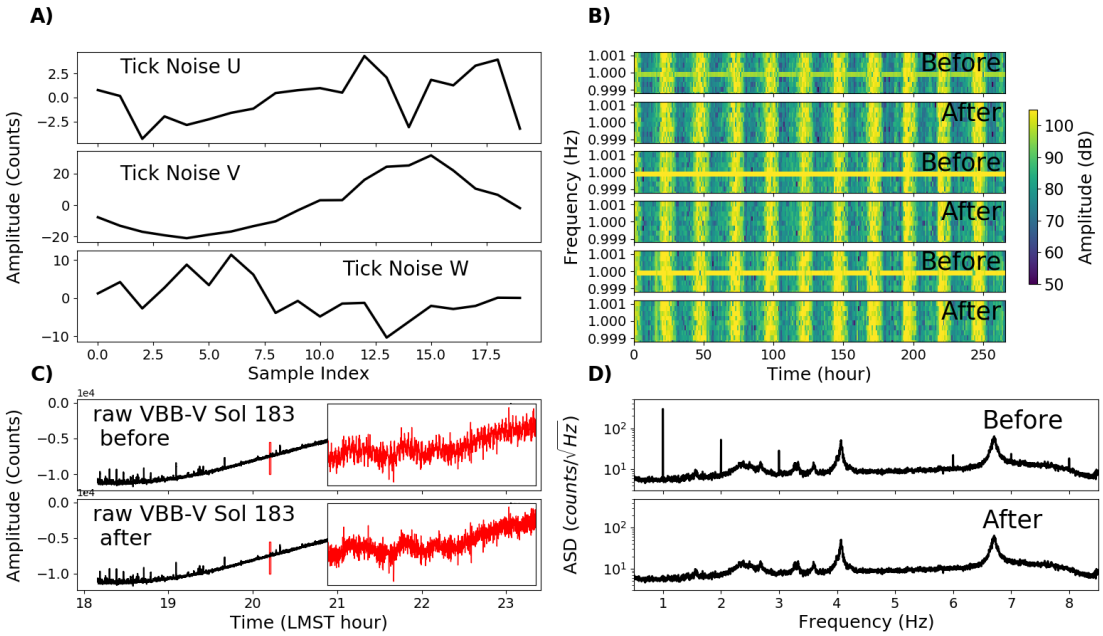

Figure 4. A) Waveforms of the estimated tick noise on the components U, V and W of the 20sps VBB channel. B) Resulting spectrograms around 1Hz of the corresponding components before and after the tick noise-removal processing. The spectrograms have a 1 hour time resolution and are closely centered around the fundamental frequency of the tick-noise at 1Hz. C) Raw VBB-V for the Sol 183 between 18:00 and 23:00 LMST before and after the tick-noise removal. The thumbnails show a zoom in the time-series corresponding to the red rectangle. D) Corresponding Amplitude Spectral Density (ASD) of the time-series in C).

2.4.2 Pre-processing : Removing the glitches

As described by Lognonné et al. (2020) (Supplementary Discussion 5), the term "glitch" refers to a particular type of signal in the seismic channels of SEIS whose wave-

form in the raw data is similar to the response of the instrument to a step in acceleration. Glitches are broadband signals but most of their energy is localized in the low frequency band (< 1Hz). A high frequency precursor can also be present at the beginning of some of them. The amplitudes of all the detected glitches extend over six orders of magnitude. They have been observed to happen at all times of each Sol but those with the highest amplitudes seem to occur at particular temperature (Scholz et al., 2020). Polarity analysis suggests that glitches have preferential polarization in the directions of the feet of the WTS, the feet of the LVL and the LSA/tether (Lognonné et al., 2020; Scholz et al., 2020). The fact that the occurrence of some glitches is temperature-related can be an issue for passive seismic applications. Indeed, if the time delay between glitches shows some regularity and glitches reproduce at fixed temperature conditions during each Sol, they could eventually interfere constructively in the autocorrelation functions.

To mitigate the risk of contamination by glitches, we employ a glitch-removal algorithm (Scholz et al., 2020) on the raw data that removes the low-frequency waveform of the most energetic glitches. We show in Figure 5 how this algorithm works. In Figure 5.A, we show the locations of the detected glitches for a representative Sol. We see that the algorithm detects more glitches during the evening when the noise level is lower. As the detection is based on template-matching, the detection threshold is more often reached during this period. In Figure 5.B we show the time-series after glitch-removal (red line) for a particular glitch with a high-frequency precursor during this Sol. We see that only the low-frequency part of the glitch is removed but not the high-frequency precursor. In Figure 5.C, we show the number of glitches that have been removed for each Sol with the algorithm used in this study. As the algorithm does not perfectly remove all the glitch waveforms, the effect of the remaining glitch signature is discussed in part 4.1.

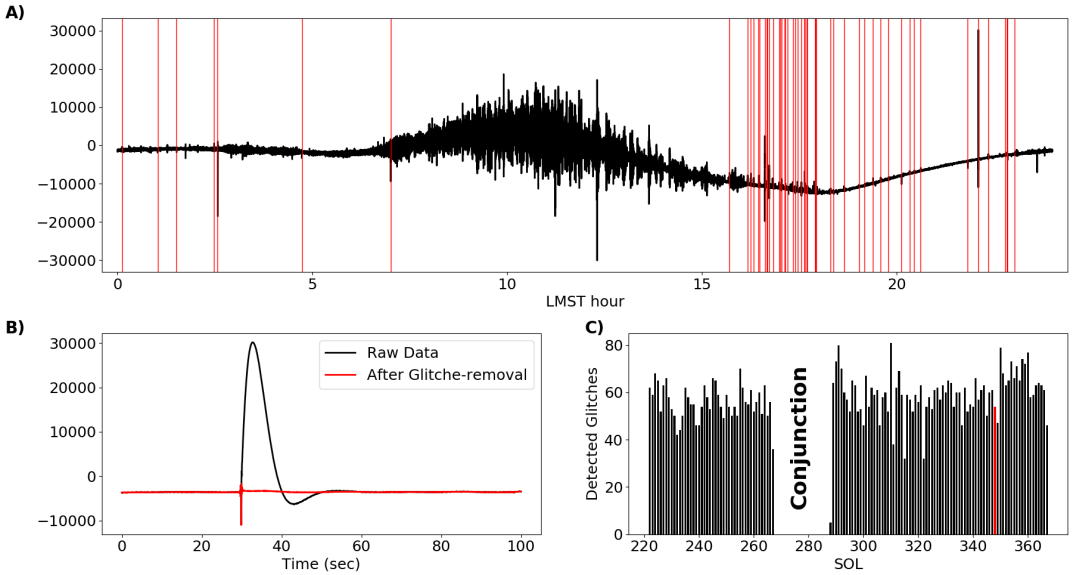

Figure 5. A)V-Component of raw 20sps-VBB data during Sol 348. Each vertical red line corresponds to a glitch detected by the glitch-removal algorithm. B) Raw data before and after glitch-removal processing for one glitch of Sol 348. C) Number of detected glitches on the V-component for all the Sols processed in this study. Sol 348 is marked by a red bar. The conjunction corresponds to a period without data during which Mars was hidden from Earth by the Sun.

2.4.3 Computation of the autocorrelation Functions (ACF)

For the ACF computed on the ambient noise, we apply a workflow similar to the one described by Bensen et al. (2007). After the tick-noise and glitch-removal processing, the instrument response is removed and the traces are rotated to the ZNE coordinate system and cut to a time duration of one Sol. For each Sol, we process independently each hour expressed in LMST (Local Mean Solar Time), in order to check the stability of the ACF in the time domain. We use this hourly stability to identify the phases in the ACF that are related to environmental contamination coming from the lander modes, thermal cracks or glitches that are varying with local time. For each sub-trace corresponding to the available data in the time window, we first remove the mean and trend using a 2nd degree polynomial fit. Next, we apply a different processing for the cross-components (ZN, ZE, EN) and for the diagonals components (ZZ, NN and EE) following the workflow of De Plaen et al. (2016).

For the diagonal components of the autocorrelation tensor, the traces are band-passed and subdivided into sub-windows of 60 seconds duration with 70% of overlap. A 1-bit normalization is applied to enforce stationnarity and improve the signal-to-noise ratio (SNR) (Bensen et al., 2007; Ito & Shiomi, 2012). Following De Plaen et al. (2016), we do not apply any spectral whitening. By definition, the phase spectrum of the diagonal components is equal to zero. All the temporal information is contained in the amplitude spectrum. They are thus very sensitive to all the modifications applied to the spectral content. Finally, we compute the full normalized autocorrelations in the spectral domain for each of these 60 second-long traces, and we stack them to obtain the ACF for the given LMST hour and the given Sol.

For the cross-components, the process is similar but here a classical spectral whitening is applied before 1-bit normalization using an apodization with a cosine-square window in the bandwidth of interest. Depending on the bandwidth and the components involved, we also apply several notch filters to remove the disturbances caused by the lander modes. For the ACF computed on the coda of the seismic events, the processing is almost identical. The various seismic events are considered as different Sols and the first subdivision into LMST is obviously not applied.

2.4.4 Computation of the Signal-to-Noise Ratio (SNR)

In order to check the stability of the various phases over the correlation time-lag we use the definition of the Signal-to-Noise Ratio (SNR) given by Clarke et al. (2011) based on a method of Larose et al. (2007). This SNR is a function of N, the number of realizations (to be defined below), and t, the correlation time-lag as:

$$SNR(N,t) = \frac{s(N,t)}{\sigma(N,t)} \tag{1}$$

With $s(N,t) = \|\langle acf(t)\rangle + i\mathbf{H}(\langle acf(t)\rangle)\|$ and $\sigma(N,t) = \sqrt{\frac{\langle acf(t)^2\rangle - \langle acf(t)\rangle^2}{N-1}}$. $s(N,t)$ is the envelope of the stacked autocorrelation function (acf) ; $\mathbf{H}$, the Hilbert transform and $\sigma(N,t)$ is the amplitude of the residual fluctuation over the number of realizations. We smooth this time-dependent SNR using a moving time window. For the frequency band investigated in the following sections we choose a width for the smoothing window equal to 2.5s for the 0.4-1Hz band, to 0.5s for the 1-2Hz and 1-3Hz bands and to 0.25s for the 3-6Hz and 4.5-7Hz bands. Clarke et al. (2011) found that a SNR of 5 is required to perform an accurate monitoring of the velocity variations with passive seismic interferometry. This value of 5 has no particular physical meaning for the autocorrelation functions of the present study but we choose to use this threshold as a comparison point between our various datasets.

We show in Figure 6 how we used this SNR to assess the stability of the phases observed in the ACF. We compute the SNR along the columns of the correlogram (they

correspond to the realizations) and we smooth it using a moving window of 10 points (0.5 sec). We show at the bottom of Figure 6.A the distribution of the SNR value in each window (colored background) and the resulting mean SNR (red line). We see that the phases visible on the correlogram and on the stack around 6 sec., 12 sec. and 21 sec. correspond to peaks of the mean SNR. On Figure 6.B, we show the resulting mean SNR (in color) for each hour of the day expressed in LMST. We see that the most energetic arrivals (at 6, 12 and 21 sec.) are clearly visible and stable during the nighttime (17:00 LMST to 06:00 LMST), particularly during the evening (17:00 LMST to 23:00 LMST). This is during this period of the martian days when atmospheric noise is the lowest. On the other hand, during daytime (06:00 LMST to 17:00 LMST) when the atmospheric noise is the strongest, no phases are visible in the ACF.

Regarding the ACF computed on the coda of the seismic events, the observed SNR is expected to be smaller. First, the SNR as defined in equation (1) increases with N, the number of realizations and the number of events which is, even from an optimistic point of view, still two times smaller than the number of Sols. Secondly, as explained by Hillers and Campillo (2016), the waveforms of the ACF computed on the coda of various seismic events could be highly variable. The convergence towards the Green's function is only achieved by averaging over a sufficiently large number of events. We suggest that this SNR analysis could however bring also some information on the similarity between the various events in terms of scattering level, source function and hypocentral distance but this goes beyond the goals of this study.

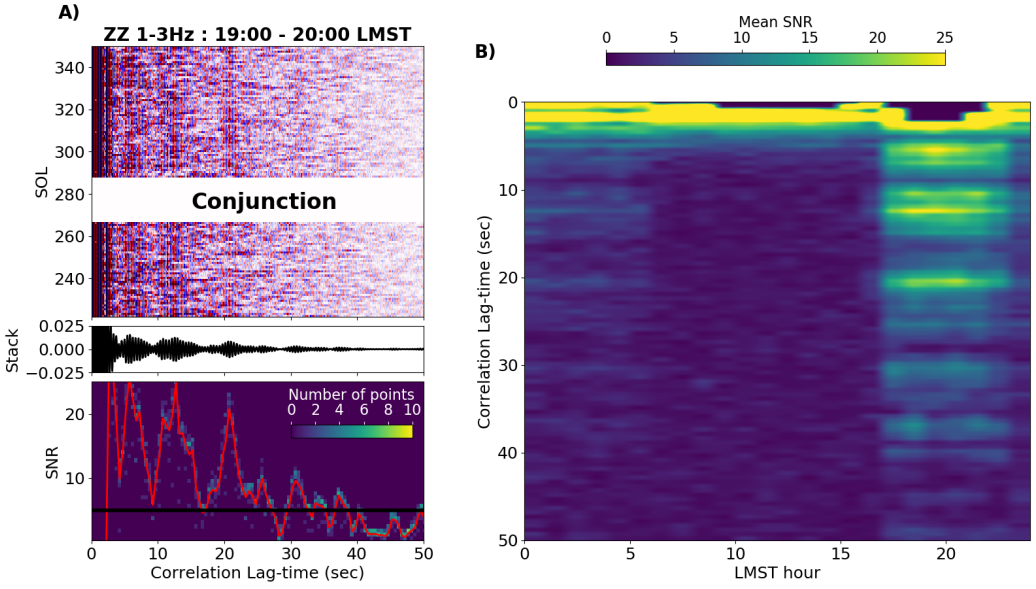

Figure 6. A) From top to bottom : Correlogram of the ZZ ACF computed for each Sol between 19:00 and 20:00 LMST in the 1-3 Hz bandwidth (color code provides amplitudes) ; Resulting stacked ACF ; Mean SNR (red line) as a function of the ACF lag-time, following the method of Clarke et al. (2011). The black line corresponds to the threshold SNR=5. The colored background represent the SNR distribution in each 10 samples-moving-windows . B) Mean SNR as a function of LMST (Local Mean Solar Time) for the ZZ component filtered between 1 and 3Hz.

3 Results

3.1 Analysis of background SEIS signals

The autocorrelation functions (ACFs) coming from ambient noise are computed in four different bandwidths : 0.4-1 Hz, 1-2 Hz, 1-3 Hz and 3-6 Hz. The low-frequency band 0.4-1 Hz does not appear to contain lander modes. However, it is more sensitive to residual glitch signals. The 1-2Hz and 1-3Hz bands contain a lander mode around 1.6Hz but this one is mainly polarized on the horizontal components. As a consequence, a notch filter centered at 1.6 Hz, which corresponds to the frequency of the lander mode averaged over one Sol, is applied to these components. The 3-6Hz band contains two lander modes at 3.3Hz and 4Hz visible on the three components. Two notch filters are consequently applied to the Z, $N$and E traces during the pre-processing.

The SNR and power spectra of the resulting ACFs are shown in Figure 7 for the ZZ component. The high SNR values (in red) near the 0 lag-time are interpreted to be due to the noise source function. No structural information can thus be extracted from this part of the ACF. We see on Figure 7 that outside of this part near the 0 lag-time, the SNR is close to zero everywhere except in the 1-3 Hz bandwidth between 17:00 LMST and 23:00 LMST.

During each Sol, the evening is known to be the period where the noise coming from the atmospheric disturbances is the lowest. It is thus in this time of the day that the seismic ambient noise can predominate. It is not surprising that we observe the best signal-to-noise ratio in this time-window. The second peculiarity of this frequency band is the presence of the 2.4Hz resonance. We see on the corresponding spectrum in Figure 7 that this resonance dominate the frequency content of the ACF during nighttime. In contrast to all the lander modes, the 2.4Hz resonance does not vary with the temperature and is also excited by the seismic events (Giardini et al., 2020). This suggests that it could be a local ground amplification. Our interpretation is that the 2.4Hz resonance amplifies the background noise at the InSight's landing site allowing a better reconstruction of the zero-offset global reflection response.

The hourly ACFs in the 1-3Hz bandwidth are very stable through the evening and point towards four predominant phase arrivals. A first arrival around 6 seconds of lag-time, a second packet with two arrivals around 10 sec and 12 sec and a last arrival around 20 sec. These arrivals are also somewhat visible in this frequency band during the morning hours (00:00 LMST to 06:00 LMST) when the atmospheric noise is higher but still below its daytime levels. The arrivals around 10 and 20 seconds can also be observed with a lower temporal resolution in the evening ACFs computed in the 1-2Hz bandwidth.

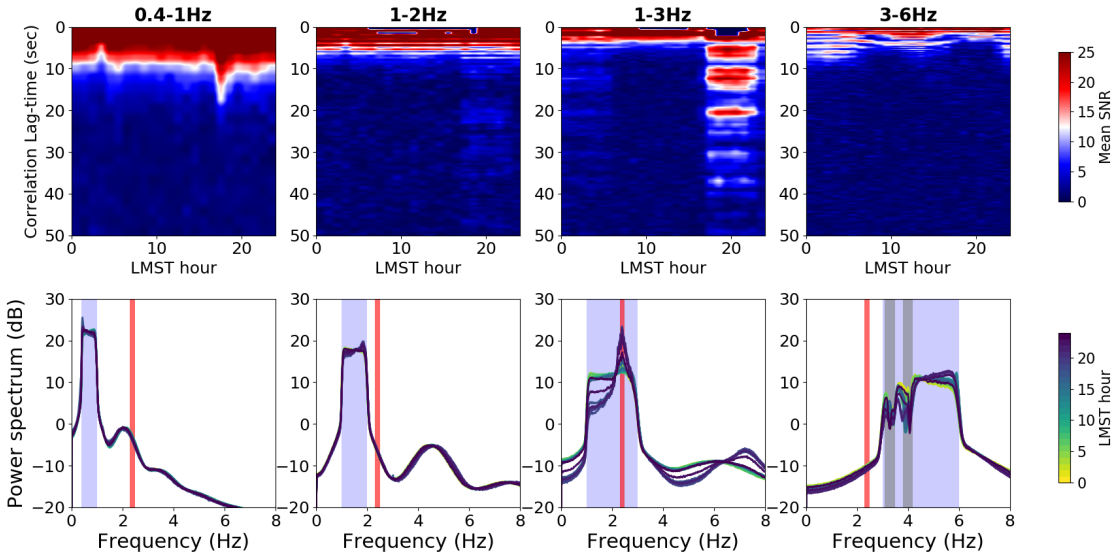

Figure 7. (Top) Mean SNR as a function of LMST for the ZZ component of the autocorrelation tensor in four different bandwidths. (Bottom) Corresponding spectral content as a function of LMST. On each subplot, the red rectangle shows the position of the 2.4Hz resonance and the blue rectangle corresponds to the bandwidth employed. The frequency bands of the notch filters applied to remove the lander modes from the data are delimited by grey rectangles.

3.2 Analysis of seismic events records

The diversity of events in terms of frequency content allows us to compute the autocorrelation functions (ACF) in several frequency bands (Figure 3). We use the Broad-Band (BB) and Low Frequency (LF) events to investigate the 0.4-1Hz bandwidth. For the 2.4Hz events we investigate the 1-2Hz and 1-3Hz bandwidths. For the High Frequency (HF) and Very-High Frequency (VHF) events we investigate three high frequency bandwidths at 1-3Hz, 3-6Hz and 4.5-7Hz. We show in Figure 8 the ZZ autocorrelation functions obtained for each of these frequency bands. We show the autocorrelation functions obtained for each particular event, the resulting stacked function and the mean Signal-to-Noise Ratio (SNR).

It has been shown in various studies (Weaver & Lobkis, 2005; Sánchez-Sesma & Campillo, 2006) that the quality of reconstruction of the Green's function with passive methods depends, amongst other things, on the amount of data used, the central frequency and the observed lag-time. In particular, this quality decreases with increasing central frequency and correlation lag-time. This has to be taken into account for the interpretation of seismic arrivals. Since (1) the number of BB-LF events is relatively small and (2) the two high frequency bandwidths 3-6Hz and 4.5-7Hz are more difficult to retrieve at long lag-time, we are more confident in the ACFs computed in the 1-3Hz bandwidth using the 2.4Hz events and the HF-VHF events. Moreover, the observed SNR is larger for these two ACFs and the two waveforms are very similar. The average ACF computed in the 1-2Hz bandwidth on the 2.4Hz events shows good agreement with the average ACF in the 1-3Hz bandwidth, in particular for the arrivals around 10.5 s and 21 s. The arrival around 10.5 s is also visible on the waveform of the 0.4-1 Hz average ACF, and marked by a tiny peak of SNR which reaches the threshold ($SNR = 5$) in the 3-6 Hz bandwidth.

The average ACFs and SNR in the 4.5-7Hz and the 3-6Hz bandwidths also present several similar peaks around 4 and 6 seconds.

The same analysis has been conducted for ACFs of horizontal components and for cross-component correlations. These results are described in the next section, which combines the results obtained from background SEIS signal and from seismic events.

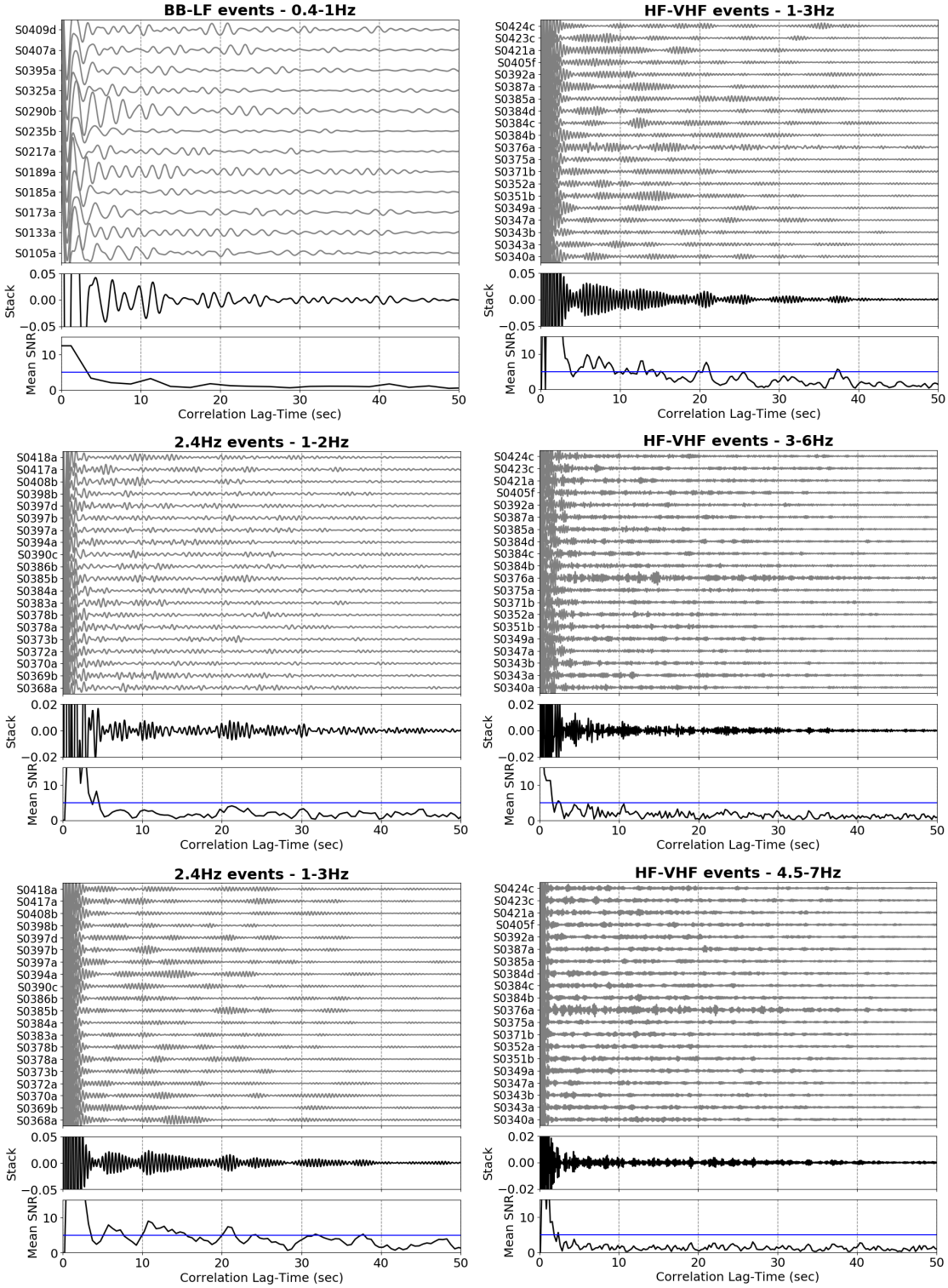

Figure 8. autocorrelation functions (ACFs) of the vertical component (ZZ) of the VBB seismometer obtained using the diffuse part of the event waveforms in various frequency bands. From top to bottom in each subplot : the ACF computed for the various events (labeled by name), the resulting average autocorrelation function and the mean SNR over the correlation lag-time. The blue line corresponds to SNR=5. 7 Low-Frequency (LF) and 5 broadband (BB) events are used all in all (all displayed). 69 2.4Hz events are used all in all (20 displayed). 39 high frequency (HF) and 16 very high frequency (VHF) events are used all in all (20 displayed).

3.3 Combined results

As expected, the mean SNR computed on the Marsquake waveforms are smaller than those obtained with ambient noise in the 1-3Hz range (compare SNR values of Figures 8 and 6). In order to compare the variations of SNR obtained for these two types of datasets, we normalize the various SNR by $\sqrt{N-1}$ to remove the dependence of the SNR on N, the number of realisations. For the three diagonal components of the autocorrelation matrix (ZZ, NN and EE), we show in Figure 9 the waveform and the normalized mean SNR of all the ACFs computed for the events and the ambient noise in the 1-3Hz bandwidth during the evening period (17:00 to 23:00 LMST).

The first thing to notice is the very good similarity between the ACFs computed in the 1-3Hz band on the ambient noise, the 2.4Hz events and the HF-VHF events for the three components. We see on Figure 8 that the autocorrelations of each individual event in this frequency band are all different. Nevertheless the stack of these events converges towards the stable waveform obtained with the ambient seismic noise. This may be related to the seismic amplification at 2.4Hz of both seismic background noise and events, in particular on the vertical component. For the ZZ ACF in the 1-3Hz range, we potentially identify at least two clear arrivals with their multiples (fig. 9). One at 6.3 seconds with its potential multiple at 12.6 seconds (green lines). The other at 10.5 seconds with its potential multiple at 21 seconds (red lines). The arrival at 6.3 seconds is also present in the high-frequency ACFs (3-6 Hz and 4.5-7 Hz ranges) and corresponds to a peak of amplitude in the 0.4-1 Hz ACF. The arrival at 10.5 seconds is also present on the 3-6 Hz ACF, the 1-2 Hz ACF and the 0.4-1 Hz ACF. These arrivals are thus validated by SNR analysis and by inter-comparison between the different data sets in various frequency bands.

For the ACFs of the horizontal components, the interpretation is less clear. For a single-station configuration in the theoretical case of a 3-D layered medium in back-light illumination, the result of Wapenaar (2003) leads to the retrieval of the vertically reflected P-waves on the ZZ component of the correlation tensor, and the vertically reflected S-waves on the NN and EE components. Nevertheless we see on Figure 9 that NN and EE are not totally similar. The three 1-3Hz ACFs have several peaks of SNR that can be observed on both NN and EE components. We have identified one primary arrival at 4.5 seconds and its multiple at 9 seconds (yellow lines) and three single arrivals (with no clear multiple) at 12.3 seconds (grey line), 14.5 seconds (violet line) and 22.4 seconds (ruddy line). The NN ACFs also present other arrivals (as manifested by peaks of SNR) that are not visible at all on the EE ACFs. At 16.2 seconds (orange line) we see a peak of SNR on the 1-3Hz ACFs and also an amplitude peak on the 0.4-1Hz ACF. However, the largest divergence between the two horizontal components occurs around 6.5 seconds (between the two yellow lines). Around this lag-time the 1-3Hz ACFs on the NN component present their most prominent peak of SNR whereas the same ACFs on the EE components are close to zero.

These differences between NN and EE could have several explanations. Firstly, the SNR appears to decrease with time much more quickly for the EE component than for the NN component. This is suggesting that the East component of the VBB record is more noisy, possibly due to a higher sensitivity to pressure perturbations (Garcia et al., 2020), or to lander noise (Murdoch, Mimoun, et al., 2017), than the North component. Secondly, the cross-components of the correlation tensor in the 1-3Hz range present some features suggesting that the East component could be disturbed by some environmental effects. We show in Figure 10 the cross-components computed on ambient noise at 1-3Hz (fig. 10.A), on HF-VHF events at 1-3Hz (fig. 10.B) and on 2.4Hz events at 1-2Hz (fig. 10.C). The two 1-3Hz ZE components present a non maximal amplitude at zero lag-time. Moreover, the EN component computed on ambient noise present a zero amplitude at zero lag-time. These features are not visible on the cross-components in the 1-2Hz range. We think that these observations are indicating an interfering signal on the

East component possibly amplified by the 2.4Hz resonance. This interfering signal could be related to the fact that the solar panels of InSight lander are aligned along the West-East axis. This could have an impact on the lander's response to the wind (Murdoch, Mimoun, et al., 2017) and to the ground vibrations. A noteworthly aspect of the cross-components of the correlation tensor is their non-zero amplitude. Indeed, in the perfect case of an horizontally layered medium, P and S waves reflecting at vertical incidence on horizontal interfaces do not produce any converted waves. The cross-terms of the Green's tensor are thus equal to zero. The non-zero amplitude of the cross-components could be related to dipping interfaces beneath the InSight's landing site, to local scattering in the medium or to seismic aisotropy.

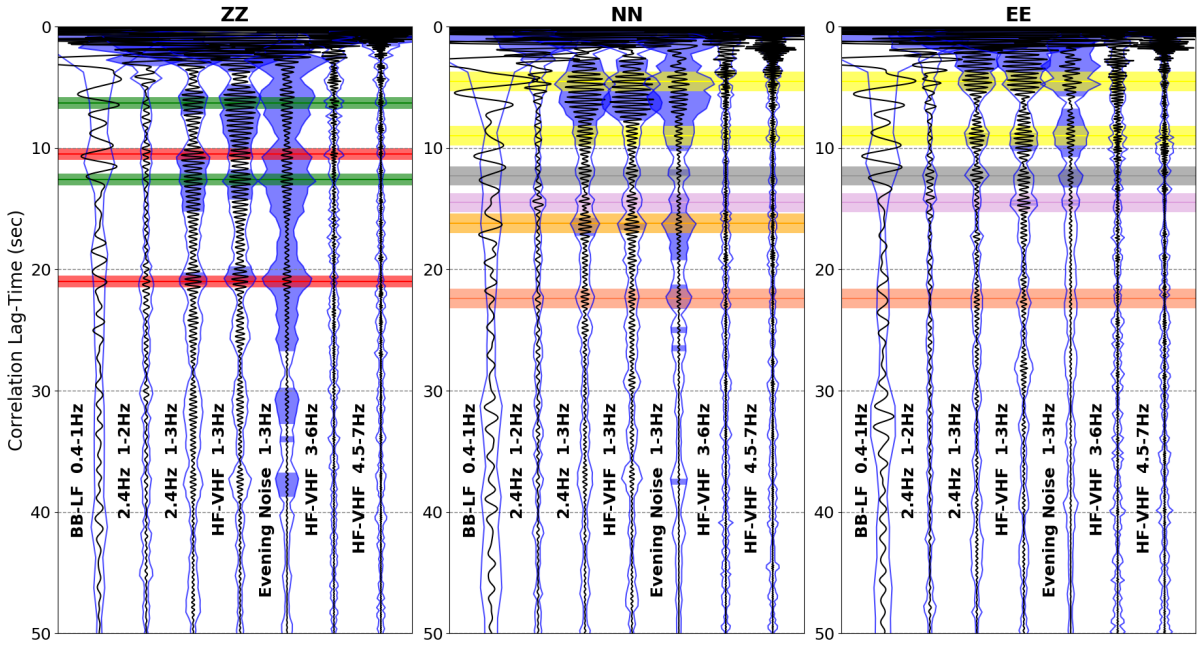

Figure 9. Waveforms of the ACF (black line) and normalized mean SNR (blue lines) for the three diagonal components of the autocorrelation tensor, and seven different datasets. The mean SNR is normalized by the square root of the number of realization in each dataset then scaled in order to be plotted with the waveform. The same scale factor is used for all the SNR (0.03). The SNR functions are represented symmetrically (blue lines) alongside each waveform. The normalized mean SNR curves are filled in blue when the non-normalized mean SNR is higher than 5. No scale factor has been applied to the various waveforms. For the ZZ component, the two green lines correspond to times 6.3 (±0.5) seconds and 12.6 (±0.5) seconds respectively. The two red lines correspond to times 10.5 (±0.5) seconds and 21 (±0.5) seconds. For the horizontal components (NN and EE) : the two yellow lines correspond to times 4.5 (±0.8) seconds and 9 (±0.8) seconds. The grey line correspond to times 12.3 (±0.8) seconds. The violet line correspond to times 14.5 (±0.8) seconds. The ruddy line correspond to times 22.4 (±0.8) seconds. The orange line only visible on NN component correspond to time 16.2 (±0.8) seconds.

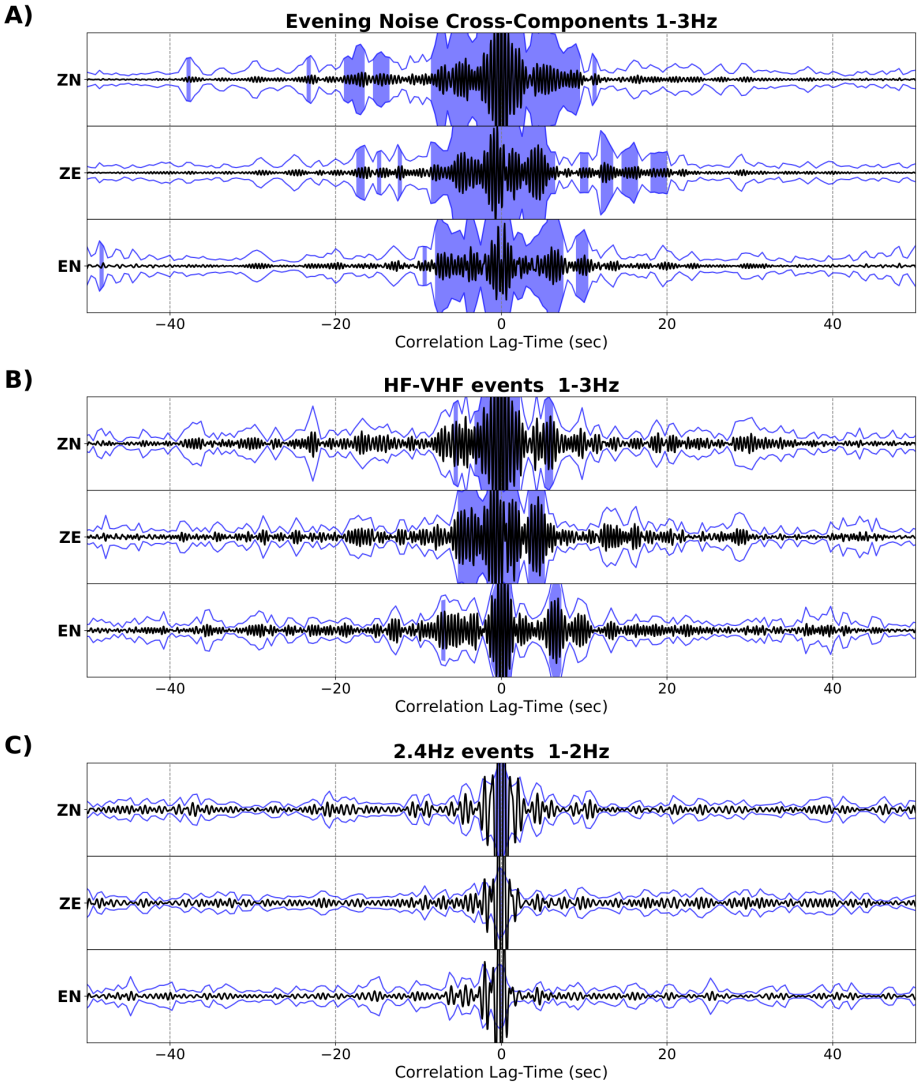

Figure 10. Waveforms of the cross-correlation functions (black line) and normalized mean SNR (blue lines) for the non-diagonal components ZN, ZE and EN for A) the ambient seismic noise between 1-3Hz averaged over the evening period ; B) the waveforms of the HF-VHF events between 1-3Hz ; C) the waveforms of the 2.4Hz events between 1-2Hz. The scale factor used for all the SNR functions is equal to 0.02. No scale factor has been applied to the various waveforms. The normalized mean SNR curves are filled in blue when the non-normalized mean SNR is higher than 5.

4 Discussion

4.1 Potential contaminations by glitches and donks

We have seen in section 2.4.2 that only the low frequency part of each glitch is removed by the glitch-removal algorithm. This implies that the temporal distribution of the glitches can still have an impact on the correlation analysis. In the same way, the distribution of donks can also contaminate the ACFs.

In Figure 11.A, we show the location of all the glitches detected by the glitch-removal algorithm in the 20 sps VBB data. They seem to be organized along particular curves on the plots. Scholz et al. (2020) have shown that these lines correspond to particular values of the temperature varying seasonally. It means that the processes behind the occurrence of the glitches are environmental and thus highly redundant. The time delay between two consecutive glitches is thus a key parameter that we have to take into account as a potential contamination of ACFs. In Figure 11.A, we show the histogram of the time delays between two consecutive glitches on the V component at different LMST. We focus our analysis on the evening part of each Sol because it is the period during which we obtain the best results with the ambient noise. We see on the histogram that the smallest delay is approximately 30 seconds and that the mean delay between two consecutive glitches is around 200 seconds. These values are too large to explain the arrivals visible on the ACFs. Moreover we see that the distribution of the delays depends on the LMST. This observation is not compatible with the stability of the arrivals over the nighttime windows.

We show on Figure 11.B the location of all the detected donks between 17:00 and 23:00 LMST from Sol 180 to Sol 261 (red crosses). This time period corresponds to the red rectangle of Figure 11.A. As the 100 sps SP data are not always available, we perform the detection of the donks on a composite SP channel called ESTASP which is available in the continuous data flow. This output is the root mean square of the vertical SP component, filtered in the 12-14Hz bandwidth and averaged over 1 second windows (Lognonné et al., 2019). The time-series of the ESTASP channel are shown in Figure 11.B. All the peaks visible on the time-series correspond to the signal of a donk. We have used a STA/LTA (1s/25s) criterion to detect these peaks automatically. In Figure 11.B (middle) we may observe three zones with a high density of donks at the beginning of the evening. These zones seem to begin at various particular Sols and extend gradually Sol after Sol. We hypothesize that the appearance of these zones is related to seasonal activations of local cracks. We see on the histogram of Figure 11.B that the delay between two consecutive donks is much smaller than the one of glitches. We see a peak around 10 seconds in the distribution of the delays between 17:00 and 18:00 LMST. This could correspond to the times of the observed phases in the ZZ ACFs on ambient noise but it cannot explain the stability of these phases over all the nighttime windows. As the distribution of the donks changes with time it cannot be the cause of the stable arrivals in the ACFs.

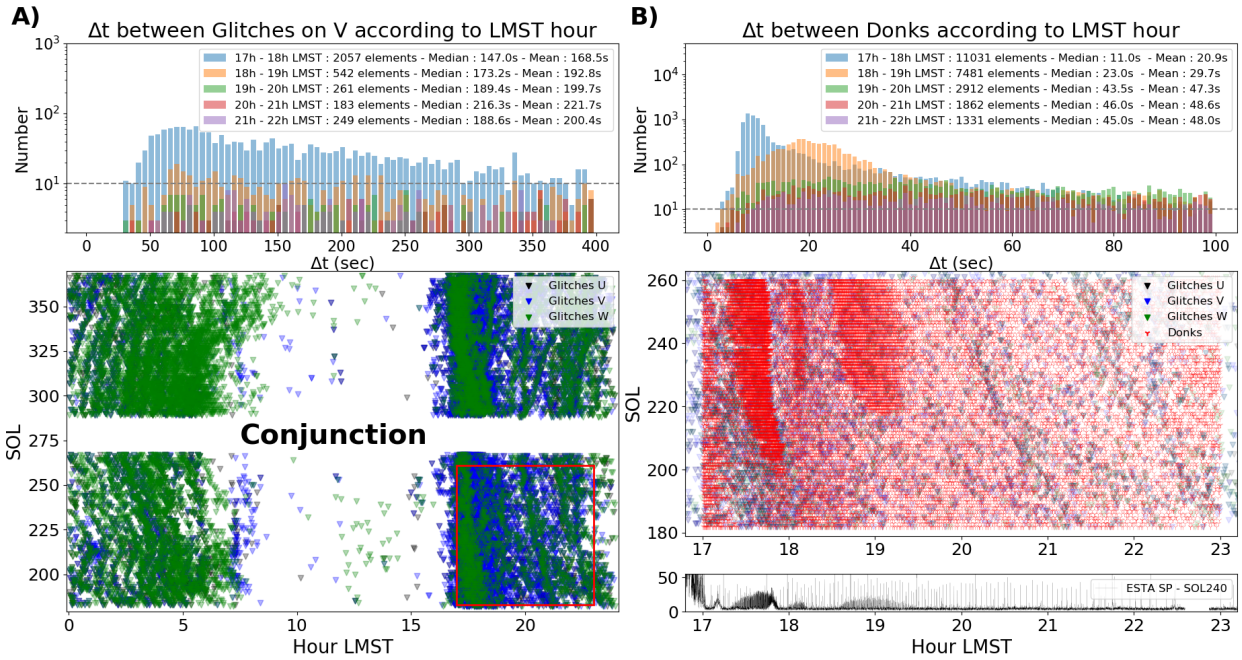

Figure 11. Distribution of glitches and donks. A) top : Histogram of the distribution of the delays between two consecutive glitches of the V component as a function of LMST. A) bottom : Time locations of all detected glitches from Sol 180 to Sol 370. As explained in part 2.4.2, the high noise level during daytime (7:00 LMST to 17:00 LMST) makes the detection less accurate. B) top : Histogram of the distribution of the delays between two consecutive donks for various LMST. B) middle : zoom in the red rectangle of the subplot A) bottom. The location in time of all the donks detected during this period are displayed in red. B) bottom : Typical time-series of the ESTASP channel from which the detection of the donks is performed.

4.2 Simulation of the spectral shape on the 2.4 Hz resonance peak of autocorrelation functions

One uncertainty concerning the autocorrelation functions computed in the 1-3Hz bandwidth is the nature of the 2.4Hz resonance. By definition the phase spectrum of an autocorrelation function is equal to zero. All the information, including the arrival time of the reflection, in the temporal waveform of the ACF are fully contained in the amplitude spectral density (ASD) of the ACF. This ASD is equal to the mean of all the power spectral densities (PSD) of the time-series used to compute the ACF. In the 1-3Hz bandwidth the spectral content is dominated by the 2.4Hz resonance (see Figure 7). Therefore, the shape of the spectrum around 2.4Hz controls the waveform of the ACF in the 1-3 Hz range. To determine if the observed shape of the 2.4Hz resonance agrees with our interpretation in terms of reflection from an interface, we performed a synthetic experiment of seismic reflection.

We consider a source function, s, defined by :

$$s(t) = \frac{e^{-\frac{(t-t_0)^2}{2T_{sig}^2}} \cos(\omega_0(t-t_0))}{\sqrt{2\pi}\sqrt{T_{sig}^2}} \tag{2}$$

We show this source in Figure 12.A with the angular frequency $\omega_0 = 2.4{\times}2\pi\, rad.s^{-1}$, the initial time $t_0 = 5\,s$ and the characteristic signal duration $T_{sig} = 0.6\,s$. To simulate a reflection we just sum the source function with a shifted and scaled version of it-

self. We obtain the signal of the Figure 12.B by adding two synthetic reflections at $t_1 = t_0 + 6.3\,s$ with the scale factor $r_1 = 0.03$ and at $t_2 = t_0 + 10.5\,s$ with the scale factor $r_2 = 0.025$. We also add some Gaussian white noise with zero mean and standard deviation 0.003.

In Figures 12.C and 12.D, we compare the autocorrelation of the synthetic signal of the Figure 12.B with the real evening ZZ autocorrelation function obtained with ambient noise in the 1-3Hz bandwidth (same as in Figure 9). Figure 12.C shows that the presence of the reflections translate into the amplitude spectrum through the appearance of small secondary peaks. Similar features are visible on the amplitude spectrum of the real autocorrelation function on Figure 12.D suggesting that the shape of the 2.4Hz resonance with several secondary peaks could be the signature of seismic reflections.

Nevertheless this synthetic test also means that all the modifications applied on the spectrum of the time-series during pre-processing can introduce some artificial phase arrivals in the ACF.

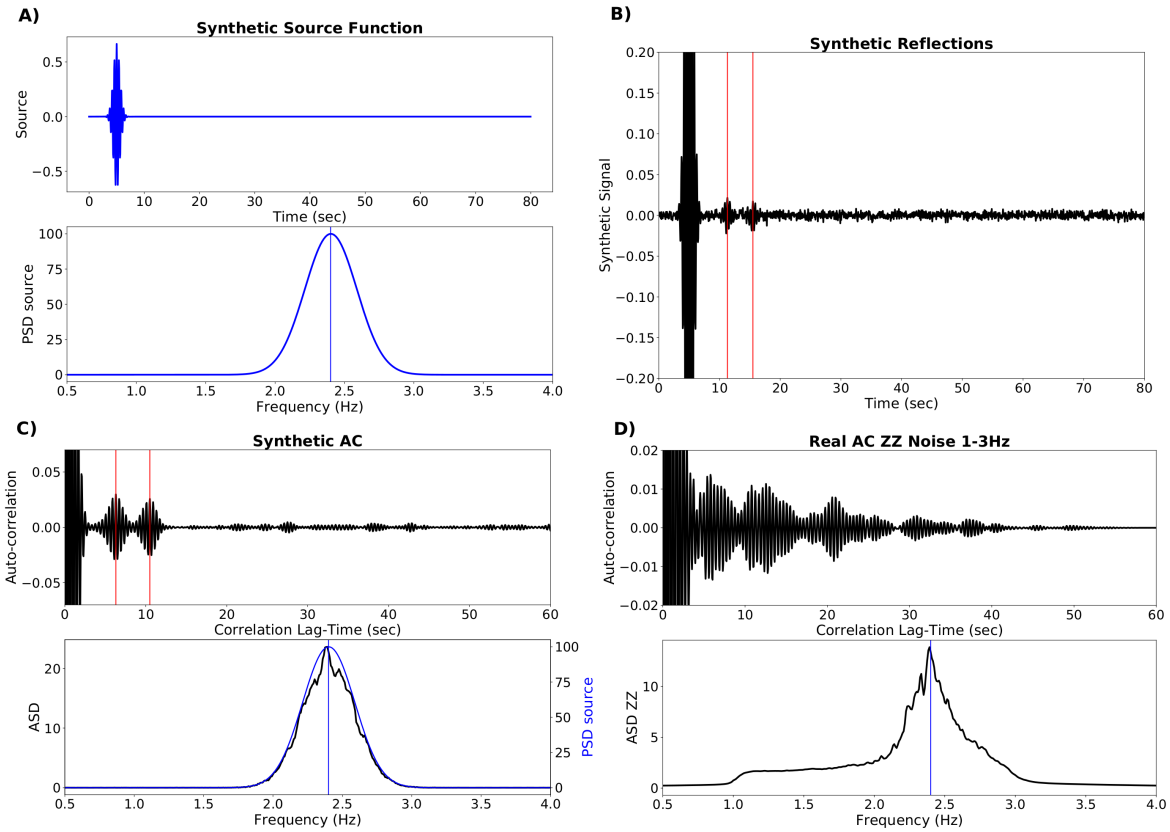

Figure 12. Synthetic experiment of seismic reflection. A) Temporal waveform and power spectral density of the synthetic source function. B) Synthetic signal with two reflections at $t_0 + 6.3\,s$ and $t_0 + 10.5\,s$ (vertical red lines). C) Temporal waveform and amplitude spectral density of the autocorrelation of the synthetic signal in B). D) Temporal waveform and amplitude spectral density of the evening ZZ autocorrelation function computed on ambient seismic noise in the 1-3Hz bandwidth.

4.3 Interpretation of the autocorrelation functions

The seismic energy arrivals with high signal-to-noise ratio visible on the autocorrelation functions ZZ, NN and EE are interpreted as vertically propagating seismic phases reflected on internal discontinuities (PdP on ZZ, SdS on Horizontal components for phases reflecting on discontinuity "d"). The most convincing seismic phases are those presenting clear multiples. On the ZZ component, we identify two phases at 6.3 seconds (multiple at 12.6 sec) and at 10.5 seconds (multiple at 21 sec). We choose here to interpret the phases at 12.6 sec and 21 sec as multiples but it could also be related to first reflection arrivals. On horizontal components we identify one phase at 4.5 seconds (multiple at 9 sec). These phases lead to a structural model of the martian crust with three main interfaces. Nevertheless, a correspondence between P-waves travel time and S-waves travel time for each discontinuity cannot be inferred clearly from our analysis due to the issues on the horizontal components. The first interface corresponding to the two way travel time at 4.5 seconds for S-waves has no unambiguous corresponding P-wave arrival on the ZZ ACF in the 1-3Hz range because the part near the zero lag-time is hidden by the source function. One potential arrival could be identified on the 3-6Hz and 4.5-7Hz ACF around 2.5 seconds (see fig. 8 and 9) that would imply a V_p/V_s ratio of 1.8. The second and third interfaces are only clearly visible on the ZZ component. Several phase arrivals on the horizontal components could correspond to the associated S-waves travel time but a structural inversion of the physical parameters is needed to infer a reliable model.

5 Conclusion

The ground velocity records of SEIS instrument have been analyzed with seismic interferometry methods. The stability analysis of the autocorrelation functions of SEIS components demonstrates that the background seismic noise signal is reliably observed only at a specific frequency (2.4 Hz resonance) and only when the environment noise is the lowest (17:00 to 23:00 LMST). The good agreement between the autocorrelation functions computed on ambient seismic noise in the 1-3Hz range and the autocorrelation functions computed on the Marsquake waveforms in other frequency bands is consistent with the interpretation of the 2.4Hz resonance as a local ground amplification due to the structure beneath the InSight's landing site. When the correlation matrix is properly resolved, its low variability as a function of local time allows us to rule out potential contaminations by artifacts, such as glitches and donks, which present strong variations with local time. The autocorrelation functions present seismic energy arrivals in the 4 to 30 seconds range that are validated by Signal to Noise Ratio (SNR) analysis and inter-comparisons between results obtained from background signal and seismic event records. In addition, some of these arrivals are presenting multiples thus favoring an interpretation as vertically propagating waves reflected on internal discontinuities. We report the possible detection of the following vertically propagating seismic waves reflected on internal discontinuities: P-waves with two-way travel times of 6.3 s (+ multiple at 12.6s) and 10.5s (+ multiple at 21s); S-waves with two way travel times of 4.5s (+ multiple at 9s). The error bar on these arrival times are estimated at $\pm$0.5s for P-waves and $\pm$0.8s for S-waves. These travel times can be used with constraints from other seismic analyses such as seismic receiver functions in order to obtain a reliable internal structure model. These results will be improved in future studies by adding new seismic events data, and by performing a full synthetic test involving full-wave simulations of the reflected phases. The weak variability of the correlation functions as a function of date will also be investigated.

Acknowledgments

This study is InSight contribution number 164. The authors acknowledge both "Université Fédérale de Toulouse Midi Pyrénées" and the "Région Occitanie" for funding the PhD grant of Nicolas Compaire. The French authors acknowledge the French Space Agency CNES and ANR (ANR-14-CE36-0012-02 and ANR-19-CE31-0008-08) for funding the

InSight Science analysis. We acknowledge NASA, CNES, partner agencies and institutions (UKSA, SSO, DLR, JPL, IPGP-CNRS, ETHZ, ICL, MPS-MPG, LPG, MSFC) and the operators of JPL, SISMOC, MSDS, IRIS-DMC and PDS for providing SEED SEIS data. SEIS data is referenced at http://dx.doi.org/10.18715/SEIS.INSIGHT.XB_2016. The Mars Quake service (MQS) catalogue of events used in this contribution is the Mars Seismic Catalogue, InSight Mission, V2 acknowledging ETHZ, IPGP, JPL, ICL, ISAE-Supaero, MPS, and the University of Bristol. It is available at http://doi.org/10.12686/a7. V. Lekic and D. Kim acknowledge support from the Packard Foundation to V. Lekic.

References

Banerdt, W. B., Smrekar, S. E., Banfield, D., Giardini, D., Golombek, M., Johnson, C. L., ... Wieczorek, M. (2020, February). Initial results from the InSight mission on Mars. *Nature Geoscience*. doi: 10.1038/s41561-020-0544-y

Bensen, G. D., Ritzwoller, M. H., Barmin, M. P., Levshin, A. L., Lin, F., Moschetti, M. P., ... Yang, Y. (2007, June). Processing seismic ambient noise data to obtain reliable broad-band surface wave dispersion measurements. *Geophysical Journal International*, *169*(3), 1239–1260. doi: 10.1111/j.1365-246X.2007.03374.x

Claerbout, J. F. (1968). Synthesis of a layered medium from its acoustic transmission response. *Geophysics*, *33*(2), 264–269.

Clarke, D., Zaccarelli, L., Shapiro, N. M., & Brenguier, F. (2011, August). Assessment of resolution and accuracy of the Moving Window Cross Spectral technique for monitoring crustal temporal variations using ambient seismic noise: MWCS: assessment of resolution and accuracy. *Geophysical Journal International*, *186*(2), 867–882. doi: 10.1111/j.1365-246X.2011.05074.x

De Plaen, R. S. M., Lecocq, T., Caudron, C., Ferrazzini, V., & Francis, O. (2016, August). Single-station monitoring of volcanoes using seismic ambient noise. *Geophysical Research Letters*, *43*(16), 8511–8518. doi: 10.1002/2016GL070078

Garcia, R. F., Kenda, B., Kawamura, T., Spiga, A., Murdoch, N., Lognonné, P. H., ... Banerdt, W. B. (2020). Pressure effects on SEIS-InSight instrument , improvement of seismic records and characterization of long period atmospheric waves from ground displacements. *Journal of Geophysical Research: Planets*.

Giardini, D., Lognonné, P., Banerdt, W. B., Pike, W. T., Christensen, U., Ceylan, S., ... Yana, C. (2020, February). The seismicity of Mars. *Nature Geoscience*. doi: 10.1038/s41561-020-0539-8

Gorbatov, A., Saygin, E., & Kennett, B. L. N. (2013, February). Crustal properties from seismic station autocorrelograms. *Geophysical Journal International*, *192*(2), 861–870. doi: 10.1093/gji/ggs064

Hillers, G., & Campillo, M. (2016, March). Fault zone reverberations from cross-correlations of earthquake waveforms and seismic noise. *Geophysical Journal International*, *204*(3), 1503–1517. doi: 10.1093/gji/ggv515

InSight Mars SEIS Data Service. (2019). *Seis raw data, insight mission.* IPGP, JPL, CNES, ETHZ, ICL, MPS, ISAE-Supaero, LPG, MFSC. Retrieved from `http://datacenter.ipgp.fr/networks/detail/XB_2016` doi: 10.18715/SEIS.INSIGHT.XB_2016

InSight Marsquake Service. (2020). *Mars seismic catalogue, insight mission; v2 2020-04-01.* ETHZ, IPGP, JPL, ICL, ISAE-Supaero, MPS, Univ. Bristol. Retrieved from `http://www.insight.ethz.ch/seismicity/catalog/v2` doi: 10.12686/A7

Ito, Y., & Shiomi, K. (2012, October). Seismic scatterers within subducting slab revealed from ambient noise autocorrelation. *Geophysical Research Letters*, *39*(19), n/a–n/a. doi: 10.1029/2012GL053321

Kennett, B. L. N., Saygin, E., & Salmon, M. (2015, September). Stacking au-

652 tocorrelograms to map Moho depth with high spatial resolution in south-
653 eastern Australia. *Geophysical Research Letters*, *42*(18), 7490–7497. doi:
654 10.1002/2015GL065345
655 Kim, D., & Lekic, V. (2019, December). Groundwater Variations From Autocor-
656 relation and Receiver Functions. *Geophysical Research Letters*, *46*(23), 13722–
657 13729. doi: 10.1029/2019GL084719
658 Larose, E. (2005). Lunar subsurface investigated from correlation of seismic noise.
659 *Geophysical Research Letters*, *32*(16). doi: 10.1029/2005GL023518
660 Larose, E., Roux, P., & Campillo, M. (2007, December). Reconstruction of Rayleigh-
661 Lamb dispersion spectrum based on noise obtained from an air-jet forcing.
662 *The Journal of the Acoustical Society of America*, *122*(6), 3437–3444. (arXiv:
663 0710.0307) doi: 10.1121/1.2799913
664 Lognonné, P., Banerdt, W. B., Giardini, D., Pike, W. T., Christensen, U., Laudet,
665 P., ... Wookey, J. (2019, February). SEIS: Insight's Seismic Experi-
666 ment for Internal Structure of Mars. *Space Science Reviews*, *215*(1). doi:
667 10.1007/s11214-018-0574-6
668 Lognonné, P., Banerdt, W. B., Pike, W. T., Giardini, D., Christensen, U., Garcia,
669 R. F., ... Zweifel, P. (2020, February). Constraints on the shallow elastic and
670 anelastic structure of Mars from InSight seismic data. *Nature Geoscience*. doi:
671 10.1038/s41561-020-0536-y
672 Murdoch, N., Kenda, B., Kawamura, T., Spiga, A., Lognonné, P., Mimoun, D., &
673 Banerdt, W. B. (2017, October). Estimations of the Seismic Pressure Noise
674 on Mars Determined from Large Eddy Simulations and Demonstration of Pres-
675 sure Decorrelation Techniques for the Insight Mission. *Space Science Reviews*,
676 *211*(1-4), 457–483. doi: 10.1007/s11214-017-0343-y
677 Murdoch, N., Mimoun, D., Garcia, R. F., Rapin, W., Kawamura, T., Lognonné, P.,
678 ... Banerdt, W. B. (2017, October). Evaluating the Wind-Induced Mechanical
679 Noise on the InSight Seismometers. *Space Science Reviews*, *211*(1-4), 429–455.
680 doi: 10.1007/s11214-016-0311-y
681 Nishitsuji, Y., Rowe, C. A., Wapenaar, K., & Draganov, D. (2016, April). Reflection
682 imaging of the Moon's interior using deep-moonquake seismic interferometry:
683 Deep-Moonquake Seismic Interferometry. *Journal of Geophysical Research:*
684 *Planets*, *121*(4), 695–713. doi: 10.1002/2015JE004975
685 Oren, C., & Nowack, R. L. (2017, January). Seismic body-wave interferometry using
686 noise autocorrelations for crustal structure. *Geophysical Journal International*,
687 *208*(1), 321–332. doi: 10.1093/gji/ggw394
688 Phạm, T.-S., & Tkalčić, H. (2017, May). On the feasibility and use of teleseis-
689 mic *P* wave coda autocorrelation for mapping shallow seismic discontinu-
690 ities. *Journal of Geophysical Research: Solid Earth*, *122*(5), 3776–3791. doi:
691 10.1002/2017JB013975
692 Romero, P., & Schimmel, M. (2018, June). Mapping the Basement of the Ebro Basin
693 in Spain With Seismic Ambient Noise Autocorrelations. *Journal of Geophysical*
694 *Research: Solid Earth*, *123*(6), 5052–5067. doi: 10.1029/2018JB015498
695 Saygin, E., Cummins, P. R., & Lumley, D. (2017, January). Retrieval of the *P*
696 wave reflectivity response from autocorrelation of seismic noise: Jakarta
697 Basin, Indonesia. *Geophysical Research Letters*, *44*(2), 792–799. doi:
698 10.1002/2016GL071363
699 Scholz, J.-R., Widmer-Schnidrig, R., Davis, P., Lognonné, P., Pinot, B., & Garcia,
700 R. F. (2020). Detection, analysis and removal of glitches from insight's seismic
701 data from mars. , n/a–n/a.
702 Sánchez-Sesma, F. J., & Campillo, M. (2006). Retrieval of the grenn function from
703 cross-correlation : the canonical elastic problem. *Bulletin of the Seismological*
704 *Society of America*, 1182–1191.
705 Tibuleac, I. M., & von Seggern, D. (2012, April). Crust-mantle boundary reflectors
706 in Nevada from ambient seismic noise autocorrelations: Crust-mantle boundary

reflectors in Nevada. *Geophysical Journal International*, *189*(1), 493–500. doi: 10.1111/j.1365-246X.2011.05336.x

Wapenaar, K. (2003, September). Synthesis of an inhomogeneous medium from its acoustic transmission response. *GEOPHYSICS*, *68*(5), 1756–1759. doi: 10.1190/1.1620649

Weaver, R. L., & Lobkis, O. I. (2005, June). Fluctuations in diffuse field–field correlations and the emergence of the Green's function in open systems. *The Journal of the Acoustical Society of America*, *117*(6), 3432–3439. doi: 10.1121/1.1898683

Wegler, U., & Sens-Schönfelder, C. (2007, March). Fault zone monitoring with passive image interferometry. *Geophysical Journal International*, *168*(3), 1029–1033. doi: 10.1111/j.1365-246X.2006.03284.x